Radiometric and spectral stray light correction for the Portable Remote Imaging Spectrometer (PRISM) coastal ocean sensor

Justin M. Haag*, Byron E. Van Gorp, Pantazis Mouroulis, David R. Thompson

Jet Propulsion Laboratory, California Institute of Technology, Pasadena, California, USA

ABSTRACT

The airborne Portable Remote Imaging Spectrometer (PRISM) instrument is based on a fast (F/1.8) Dyson spectrometer operating at 350-1050 nm and a two-mirror telescope combined with a Teledyne HyViSI 6604A detector array. Raw PRISM data contain electronic and optical artifacts that must be removed prior to radiometric calibration. We provide an overview of the process transforming raw digital numbers to calibrated radiance values. Electronic panel artifacts are first corrected using empirical relationships developed from laboratory data. The instrument spectral response functions (SRF) are reconstructed using a measurement-based optimization technique. Removal of SRF effects from the data improves retrieval of true spectra, particularly in the typically low-signal near-ultraviolet and near-infrared regions. As a final step, radiometric calibration is performed using corrected measurements of an object of known radiance. Implementation of the complete calibration procedure maximizes data quality in preparation for subsequent processing steps, such as atmospheric removal and spectral signature classification.

Keywords: imaging spectroscopy, Dyson spectrometer, coastal ocean, instrument calibration

1. INTRODUCTION

The Portable Remote Imaging Spectrometer (PRISM) was designed to achieve the demanding goals of visible/near-infrared (VNIR) imaging spectroscopy science applications [Mouroulis et al. 2014]. Highly variable coastal ocean scenes require spectral resolution of less than 5 nm and spatial resolution on the order of meters. High signal-to-noise ratio (SNR) is required due to low reflected signal from dark water targets. Sand and ocean glint typically have much higher reflectance than that of deep water, so sufficient dynamic range is needed to capture the full range of expected scene radiance. The ultimate quantity of interest is generally remote sensing reflectance (R_{RS}), which requires the simulation and removal of atmospheric effects, so that the residual signal may a fraction of the collected radiance. Once R_{RS} is obtained, higher level data products may further reduce the signal, for example in the estimation of benthic reflectance, where radiative transfer through the water column is modeled and those effects removed [Thompson et al. 2017a].

To meet the above performance requirements, PRISM was designed as a pushbroom imaging spectrometer with high uniformity, low polarization sensitivity, and high SNR over a wavelength range of 350 to 1050 nm. A two-mirror telescope is paired with a fast F/1.8 Dyson form spectrometer (Fig. 1), utilizing a concave grating and slit fabricated by the Microdevices Laboratory at JPL. Raw data from a Teledyne HyViSI 6604A detector array is read out at 167 frames per second, enabling high SNR and dynamic range, even at typical airspeeds, by averaging multiple frames. The detector array is read out as four individual panels, each with 160 spatial pixels and 285 spectral pixels at 27 µm pixel pitch. This approach requires special consideration during data processing to mitigate electronic artifacts caused by electrical crosstalk between panels. An order-sorting filter (OSF), consisting of a combined long-pass and short-pass filter is bonded to the front surface of the detector array. For pixels away from the seam, the OSF can be considered as two independent filter segments. The optomechanical assembly is contained in a vacuum housing, which is mounted with vibration isolators on an aircraft-compatible plate and paired with an INS/GPS to enable geolocation of field data. The optical head is then installed into an aircraft along with associated focal plane and thermal control electronics, and a flight computer for recording data frames and associated telemetry.

Corresponding author: *justin.haag@jpl.nasa.gov; Address: Jet Propulsion Laboratory, 4800 Oak Grove Drive, MS 306-388, Pasadena, CA, USA 91109.

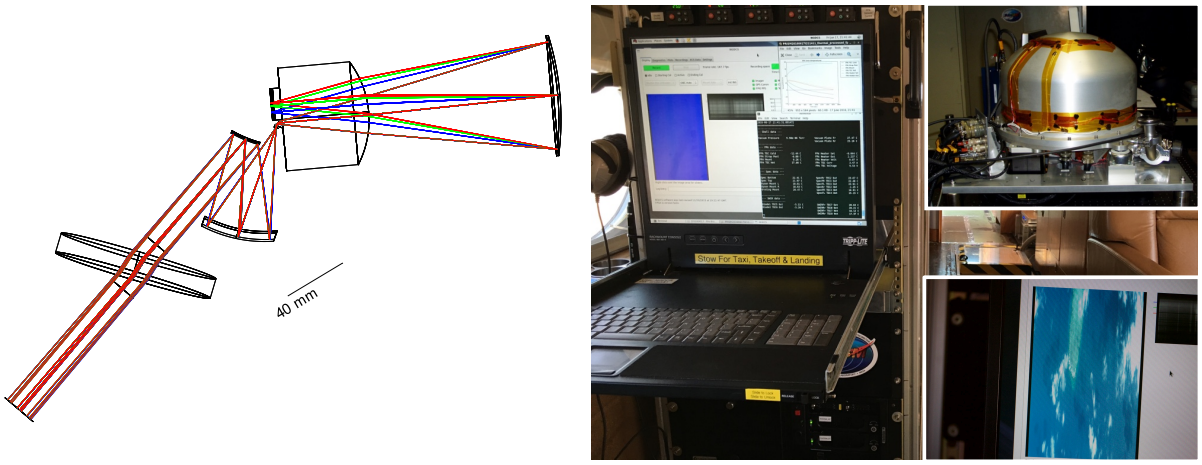

Figure 1: The airborne Portable Remote Imaging Spectrometer (PRISM).
Left: PRISM optical layout showing two-mirror telescope and F/1.8 Dyson spectrometer;
Right: PRISM flight data processing system and instrument optical head.

Since 2012, PRISM has participated in numerous field campaigns in the coastal United States, including regions of Florida and California [Heupel et al. 2012], the Southern Ocean and Antarctica during the NSF ORCAS study [Stephens et al. 2017], and the Great Barrier Reef, Hawaiian Islands, and Mariana Islands during the NASA CORAL mission [http://coral.jpl.nasa.gov/].

This paper will provide an overview of the science data processing scheme from raw data to remote sensing reflectance, with a particular focus on the estimation and correction of spectral stray light. The initial correction requires removal of electronic panel artifacts which are empirically modeled and removed from each data frame. At this point, it is possible to perform flat field and radiometric calibrations. Valid radiance and reflectance retrievals require radiometric calibration accuracy of 1% [Green 1998], so stray spectral light estimation and correction may be necessary. After obtaining calibrated radiance values, orthorectification and atmospheric removal are performed, with subsequent processing steps, e.g. glint removal, benthic reflectance retrieval, etc., to follow. The focus of the present study is on the electronic panel artifact and stray light corrections specific to the PRISM sensor, as these have not yet been described in the literature.

2. FOCAL PLANE ARTIFACT CORRECTIONS

The PRISM sensor has several sources of focal plane array (FPA) crosstalk which would cause significant artifacts in the raw and higher-level data products if left uncorrected. The PRISM FPA is read out in parallel using four separate 160x285 pixel panels, each with dedicated ADC and analog electronics, but with several shared bias reference voltages. The artifacts are primarily caused either by bias reference voltages sagging under varying loads or crosstalk between the analog signals in the four panels. Sources of these issues reside both within the FPA/readout integrated circuit (ROIC) itself and in the focal plane interface electronics (FPIE). The artifacts can be categorized as pedestal shift (PdS) or electronic panel (EP) artifacts, based on the time domain, which portion of the pixel readout is affected, and the required correction scheme. Pedestal shift (PdS) is observed when a signal on one portion of the FPA results in a uniform negative shift in signal throughout the entire FPA. The PdS artifact affects all FPA pixels read out over a single integration/frame, whereas the EP artifacts affect all spatial pixels read out for a single spectral channel over the time required to acquire 160 spatial pixels (roughly one integration time divided by 285).

2.1 Pedestal shift (PdS)

Pedestal shift (PdS) is observed when a signal is applied to the FPA, resulting in a uniform dark level decrease in each of the four FPA panels. Fig. 2 shows an average of signal over all spatial channels vs. spectral channel number while the full entrance aperture of the PRISM sensor is illuminated by an integrating sphere with quartz tungsten halogen (QTH) lamp input. The PdS artifact creates ~20 DN offset that is nearly uniform across the array. Note there is a small variance between

different panels and odd/even spatial columns which is accounted for in the correction. To demonstrate the PdS effect on masked areas of the FPA, the data in Fig. 2 was read out using the full 481x640 pixels. Pixels beyond spectral channel 273 are masked by the order sorting filter (OSF) dark mask and should therefore be nearly zero, yet it is clear that the signal has approximately linear falloff when DN is plotted in logarithmic scale. This is likely due to charge diffusion effects when illuminated with signal at wavelengths close to the FPA 1.05 µm cutoff and silicon bandgap.

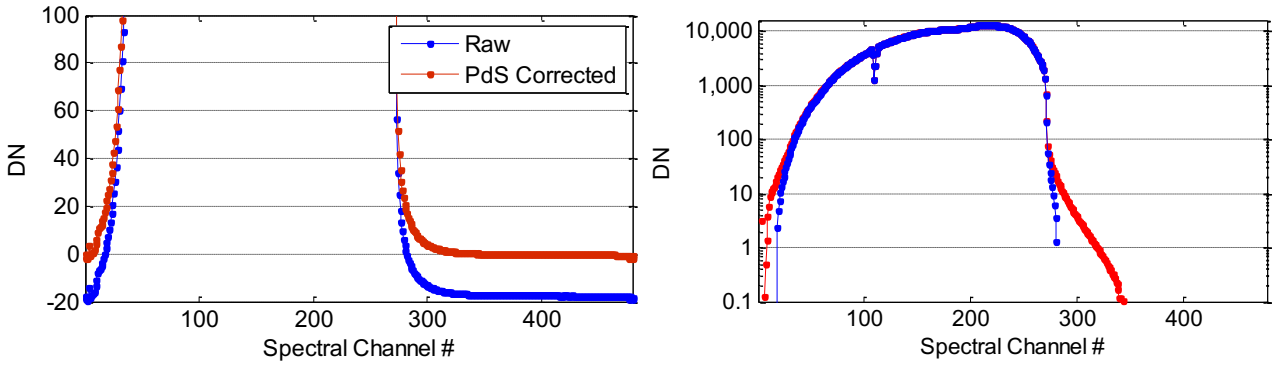

Figure 2: Example of pedestal shift (PdS) artifact. *Left:* Linear DN axis; *Right:* Logarithmic DN axis.

Typically, data from the masked pixels would be used directly to measure the shift in signal, but the PRISM masked pixels which are read out (spectral channels 274 to 285) still have significant signal related due to the charge diffusion issue discussed above. The masked pixel dark levels do not drop below 0.1 DN until spectral channel 350, well beyond the last normally read out channel (285). To correct the PdS, we postulate that the masked pixels maintain a unique shape, y_c, as function of spectral channel number. The shape of this curve is initially measured using the data in Fig. 2, and is correlated to the measured data, y_{exp}, via the equation $y_c = \alpha(y_{exp} + d_{sh})$, where α is a scale factor dependent on the signal and d_{sh} is a dark shift term directly correlated to the PdS dark signal shift. The equation above can be rearranged and represented in matrix form, yielding Eq. (2.1), where $pinv()$ is the Moore-Penrose pseudoinverse, which yields the least squares solution of parameters α and d_{sh}.

$$\begin{bmatrix} -1/\alpha \\ d_{sh} \end{bmatrix} = pinv\left(\begin{bmatrix} 1 & -1/y_{c(273)} \\ \vdots & \vdots \\ 1 & -1/y_{c(285)} \end{bmatrix}\right) \times \begin{bmatrix} y_{\exp(273)}/y_{c(273)} \\ \vdots \\ y_{\exp(285)}/y_{c(285)} \end{bmatrix} \tag{2.1}$$

The PdS parameter d_{sh} is calculated by separately using this method on all spatial channels, then averaging odd/even results for each of the four FPA panels, resulting in eight d_{sh} terms per frame which are applied on an odd/even and panel-wise basis. The correction has been validated on a variety of science and laboratory data using sources with varying illumination types, demonstrating accurate correction of the PdS artifact in all observed cases. Fig. 3 shows the effect of PdS correction on a data set collected using a small integrating sphere with white light source scanned across the instrument entrance aperture. To present only the PdS correction, the data was first corrected for electronic panel artifacts.

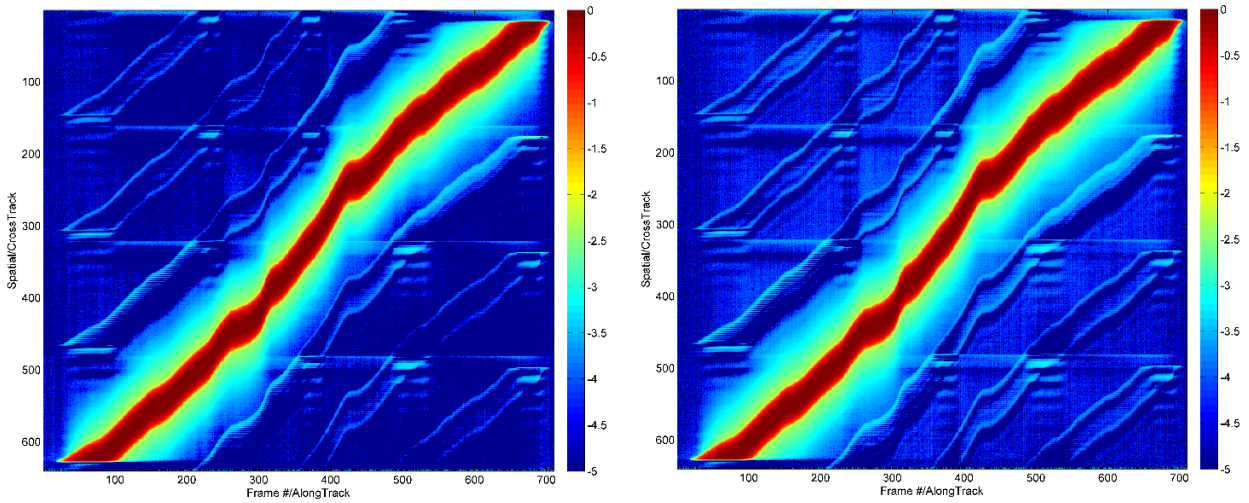

Figure 3: PRISM data scan pedestal shift (PdS) correction example. 650 nm data normalized and log scale.
Left: Before PdS correction, but including electronic panel artifact corrections;
Right: After PdS correction, which is observed as an overall intensity increase.

2.2 Electronic panel (EP) artifacts overview

Electronic panel (EP) artifacts affect the pixels read out in a single spatial row corresponding to one spectral channel. The EP artifacts include EP ghost (EPG), EP shift (EPS), and EP discontinuity (EPD). Fig. 4 shows raw and corrected data along with the EPG, EPS, and EPD components. EPG is the result of signal input in one quadrant being mirrored into all other quadrants, which is not true ghosting in the optical sense. EPG causes a negative shift in signal of pixels read out simultaneously in the other FPA panels. The shift is generally 0.2% of signal in DN of the illuminated panel. EPS is observed when spatial channels within 20 pixels of the end of any panel are illuminated, i.e. spatial pixels 140 to 160, 300 to 320, 460 to 480, or 620 to 640, resulting in a uniform shift of all 640 spatial pixels within any single spectral channel. The magnitude of the EPS shift has a nonlinear relationship, dependent on how much signal is present within 20 pixels of the panel boundary, and the contribution to the shift also increases nonlinearly when approaching the panel edge. EPD is observed as a steep discontinuity at the start of each FPA panel, and has an exponential shape that approaches zero when the moving away from the panel starting edge. It is generally negligible by 40 pixels from the panel edge. Unlike EPG or EPS, the EPD has a portion of the shift convolved into the next spectral channel, which results in spectral pixels being convolved with other spectral pixels. This is particularly problematic in regions of steep spectral slope. Each of these artifacts must be properly characterized and corrected to allow for accurate estimation of radiance L and subsequently derived quantities, such as remotely sensed reflectance R_{RS}.

The correction methods for all EP artifacts are similar. For each artifact, the desired values, e.g. DN and pixel number, are extracted from the appropriate FPA regions using data obtained with an integrating sphere with white light illuminating a small portion of the sensor field (20-80 pixels). To present the EP artifacts under varying illumination conditions, data was collected using the same integrating sphere scanned across the instrument field of view. Analytic fits are performed using the MATLAB Curve Fitting Toolbox to extract the coefficients of an exponential and/or polynomial curve that best matches the points in a least squares sense. The coefficients are stored for future use in the science data system (SDS) to process calibration and field data. For each case, the analytical fit representing the artifact is presented, along with a figure showing the effect of applying the correction.

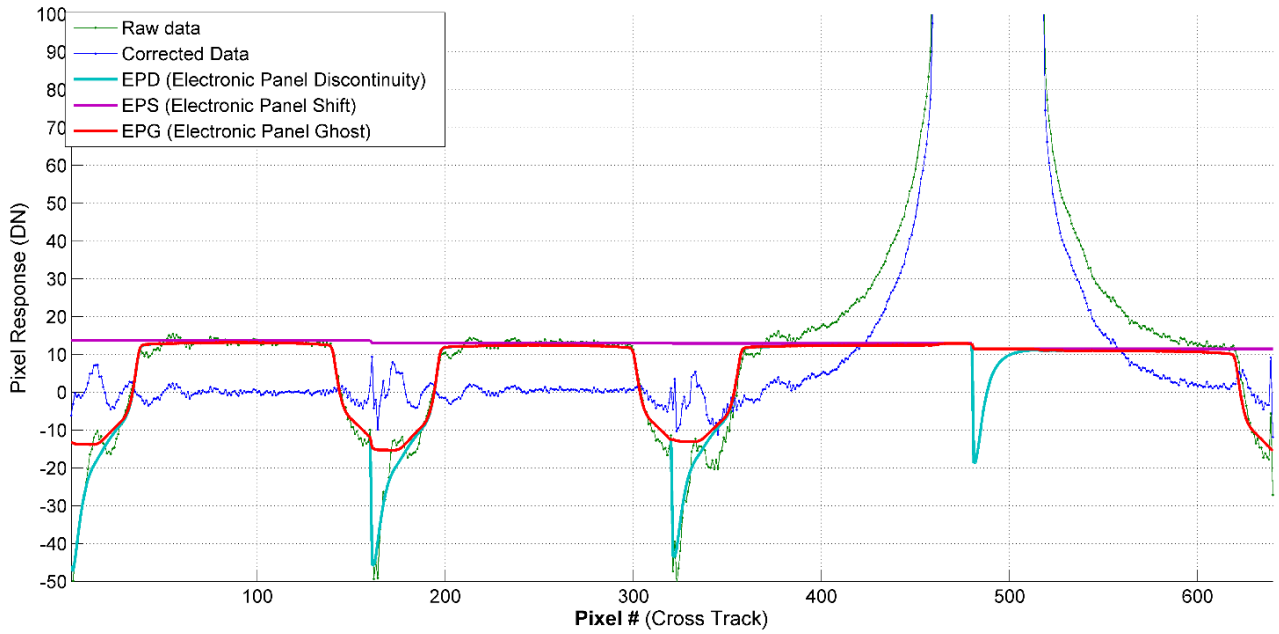

Figure 4: Example profile of PRISM electronic panel (EP) artifacts at a single wavelength (650 nm). Raw and corrected data is represented by the green and blue dotted lines, respectively. The electronic panel ghost (EPG), electronic panel shift (EPS) and electronic panel discontinuity (EPD) artifact estimates are indicated by the thick red, purple, and cyan lines respectively.

2.2.1 Electronic panel ghost (EPG)

The EPG correction is a function of DN, such that the curve fit results in a factor to be applied to a pixel, or row of pixels, depending on the DN value. The form of the fit is: $f(x) = -(Ae^{Bx} + C)D + Ex$, where x is signal in DN for any single spatial pixel. This function calculates the proportion of the signal from the i^{th} pixel in one FPA panel to be added as a shift to the i^{th} pixel in the other three panels, i.e. calculated shift for spatial pixel 40 is added to the pixels 200, 360, and 420. Fig. 5 shows the effect of the EPG correction on data that has been PdS, EPS, and EPD corrected.

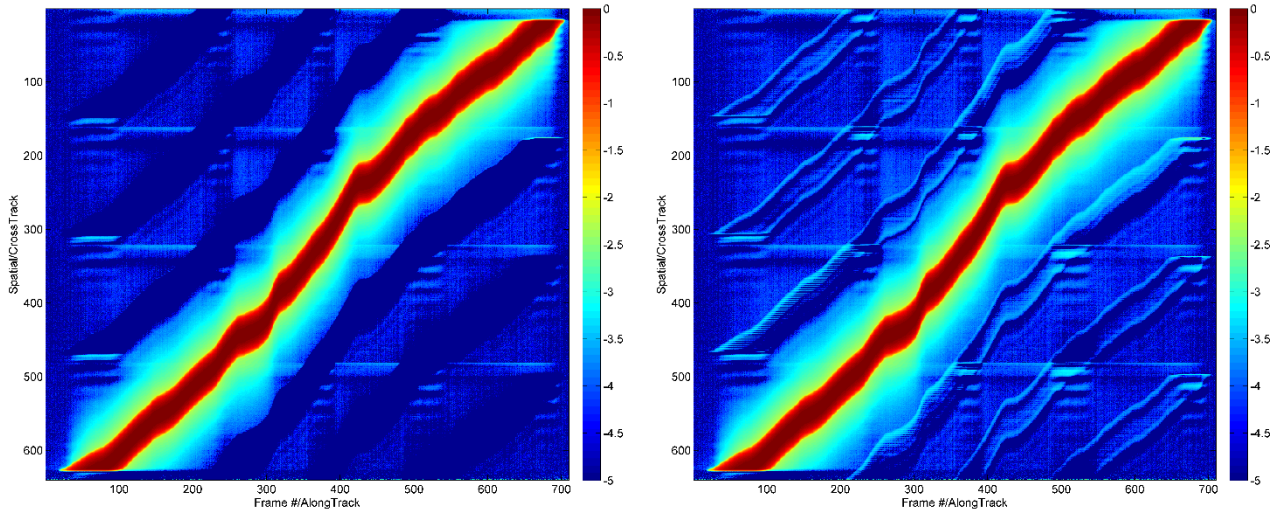

Figure 5: PRISM data scan electronic panel ghost (EPG) correction example. 650 nm data normalized and log scale. *Left:* With PdS, EPS, and EPD corrections; *Right:* After EPG correction.

2.2.2 Electronic panel shift (EPS)

The EPS correction consists of two curve fits. The first fit models the dependence of the dark shift on signal in DN. The form of the second fit is: $f(x) = A\left(\frac{X}{B}\right)^{C/2-1} e^{-\frac{x}{2B}} + D - Ex$, where x is DN. The EP shift is a cumulative operator depending on the total amount of signal in the last 20 pixels of the panel. The second curve fit is a six degree polynomial that increases nonlinearly from zero at pixel 140 until the end of the panel. It models the relative contribution from each of the pixels in the panel. The first equation is applied to the data, then multiplied by the second and summed together to result in the amount of shift to subtract. Fig. 6 shows the effect of the EPS correction on data that has been PdS, EPG, and EPD corrected.

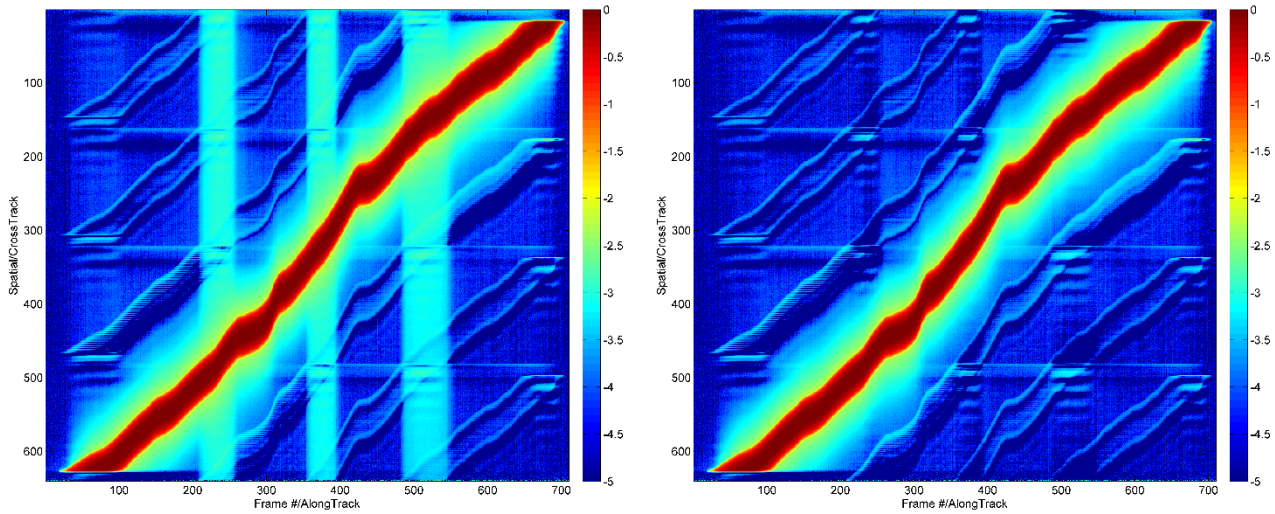

Figure 6: PRISM data scan electronic panel ghost (EPS) correction example. 650 nm data normalized and log scale. *Left:* With PdS, EPG, and EPD corrections; *Right:* After EPS correction.

2.2.3 Electronic panel discontinuity (EPD)

The EPD correction requires fitting a curve to the steep discontinuity at the start of each FPA panel (see Fig. 4). The curve fit takes the form $f(x) = \frac{(Ax^2+Bx+C)}{(x^2+Dx+E)}$, where x is spatial pixel number. The fitting process is performed once for each quadrant, resulting in a 4x4 matrix of coefficients. The magnitude of EPD shift has a linear scaling dependence on the sum of signal in DN over the spatial columns in each panel. The EPD shift is calculated by multiplying the curve fit above by the sum of signal over all spatial channels within the FPA panel (for a single spectral channel). As previously noted, the EPD has some dependence on signal levels in adjacent spectral channels but the present correction scheme does not account for this effect. Fig. 7 shows the effect of the EPD correction on data that has been PdS, EPG, and EPS corrected.

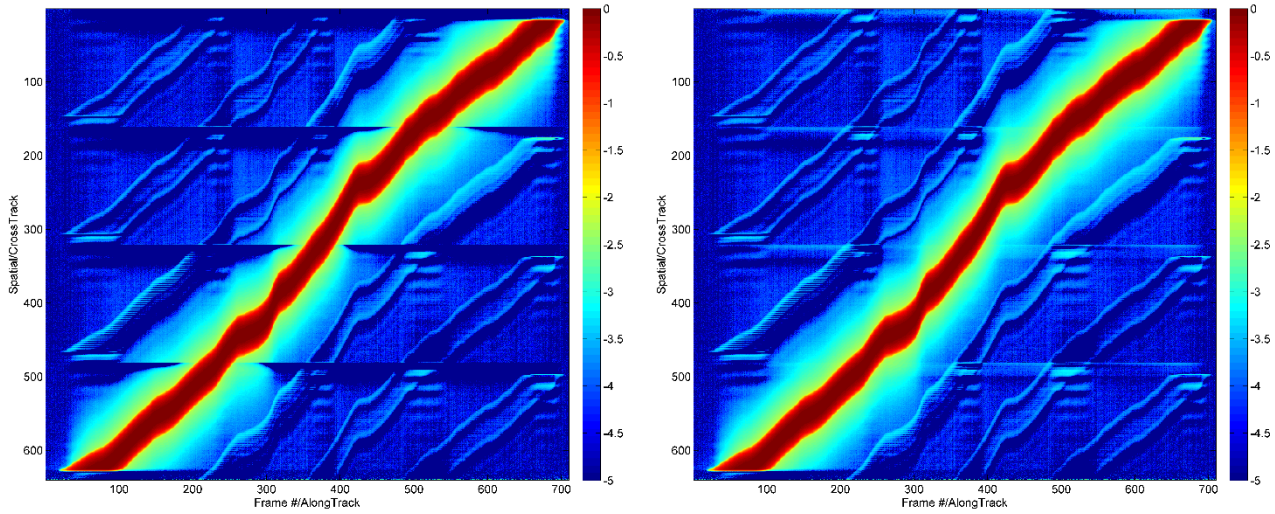

Figure 7: PRISM data scan electronic panel ghost (EPD) correction example. 650 nm data normalized and log scale. *Left:* With PdS, EPG, and EPS corrections; *Right:* After EPD correction.

3. SPECTRAL RESPONSE FUNCTION ESTIMATION

The first step of the stray spectral response correction is to determine the form of the spectral response function (SRF). This can be measured or modeled—in most cases, a combination of both methods will be required. As a first approximation, we consider an imaging spectrometer point spread function (PSF) to be separable into a spectral response function (SRF) with only spectral dependence and a cross-track response (CRF) function with only spatial dependence [Thompson et al. 2017b], measured scene radiance L has the form:

$$L_{meas} = ((L_{actual}C)^T S)^T \tag{3.1}$$

with radiance L, cross-track response matrix C, and spectral response matrix S. The 2D spectral and cross-track response matrices are generated by stacking 1D response functions, centered at the appropriate spectral or spatial position. In the present study, cross-track response will be neglected, so that $C = I$, where I is the identity matrix. Once the SRF is known and used to construct S, the spectral correction proceeds as follows, with the full correction structure preserved for reference:

$$L_{corr} = (((C^T)^+((S^T)^+ L_{meas})^T)^T)^T \tag{3.2}$$

where $A^+ = (A^T A)^{-1} A^T$, with $A^+ A = I$, is the Moore-Penrose pseudoinverse. In practice, the nominal Gaussian peak response is not removed [Zong et al. 2006], in order to maintain compatibility with downstream processing, including atmospheric removal. The SRF can then be considered as a sum of two response functions, i.e. the nominal SRF (NSRF) and stray SRF (SSRF). The SSRF will be used to correct the spectral dimension of data frames.

Furthermore, for spatially summed or averaged data, as is done for illuminated Spectralon panel frames used in the radiometric calibration, it is useful to define the line spread function (LSF), which is the integral of the PSF in one direction. Here, the spectral LSF (SLSF) will be used, which is calculated by summing the PSF in the spatial direction. Analogous terminology for nominal and stray components can also be used here, i.e. the nominal SLSF (NSLSF) and stray SLSF (SSLSF). All of these SLSF components are additionally defined in the interest of application to laser line and long-pass filter transmission data, where the data is frequently averaged in the spatial dimension. Note that the above equations apply identically when using the LSF, by collapsing the dimensions of the data frames (containing radiance L) appropriately.

Confidence in the SRF form is critical, since correction involves an inverse matrix operation that can easily corrupt data if incorrect. It is therefore necessary to validate any correction on real data. In this study, results of the stray spectral response correction are compared to ground truth reflectance collected by experienced operators using an ASD FieldSpec Pro spectrometer.

As previously described, the PRISM sensor contains an order-sorting filter (OSF) bonded to the detector surface. In the initial correction algorithm, the OSF is considered to consist of two distinct short- and long-pass filter segments, such that the SRF matrix (and similar SLSF matrix) is the sum of two matrices ($S = S_1 + S_2$), resulting from the concatenation of two response functions, each containing information only from a single filter segment (equal to zero elsewhere). This simplification is not strictly valid for pixels nearest the OSF, but methods to handle this problem, e.g. interpolation of raw data, are straightforward and will not be explored here.

3.1 Tunable laser PSF measurements

Spatially and spectrally limited data were collected using a Newport Inspire optical parametric oscillator tunable laser directed to the input of an Acton SpectraPro 500i monochromator at 8 wavelengths spanning the available instrument range, at 352 nm, 370 nm, 410 nm, 492 nm, 590 nm, 650 nm, 850 nm, and 1000 nm. Note that the slit was overfilled in the spectral direction. For each wavelength, 4 field points were collected, corresponding to spatial pixels 88, 227, 380, and 510. For each spatial and spectral location, saturated and unsaturated frames were acquired (Fig. 8), along with simultaneous power meter measurements using an irradiance sensor placed in the collimated beam path.

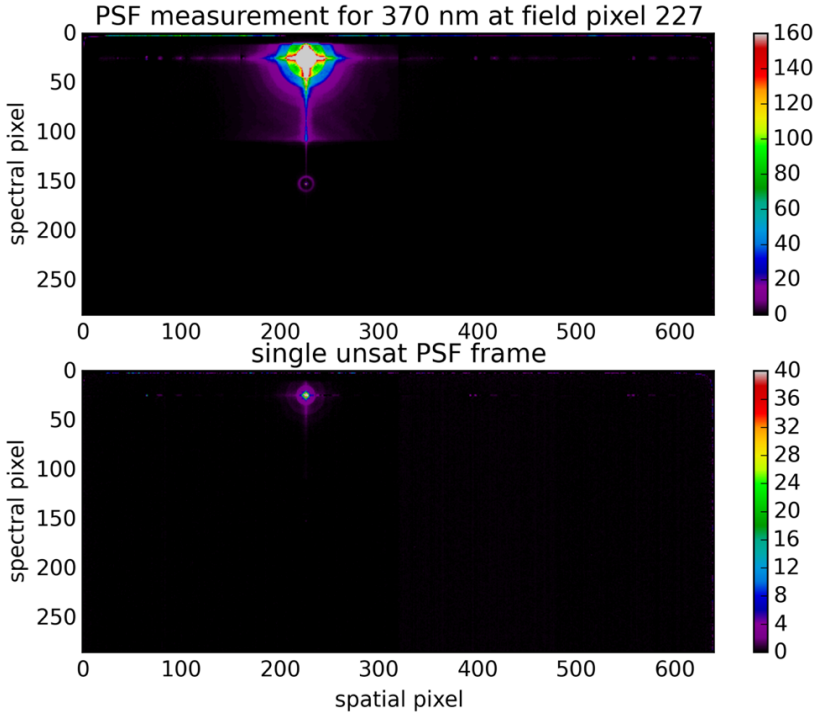

Figure 8: PRISM PSF data frames for center wavelength 370 nm and field pixel 227.
Top: Saturated data frame; *Bottom:* Unsaturated data frame.

3.2 Extract SRF and SLSF from tunable laser data

The independent power meter measurements were used to combine the saturated and unsaturated data sets. Saturated data frames were multiplied by the ratio of unsaturated to saturated power. Unsaturated data (DN < 8000) from the saturated frames was combined with data from the unsaturated frames. This same procedure was performed for the full data set, with an example result for the 370 nm measurement shown in Fig. 9. Thick black lines represent the corrected SRF (Fig. 9, left panel) and SLSF (Fig. 9, right panel) profiles used for subsequent steps in the spectral response correction.

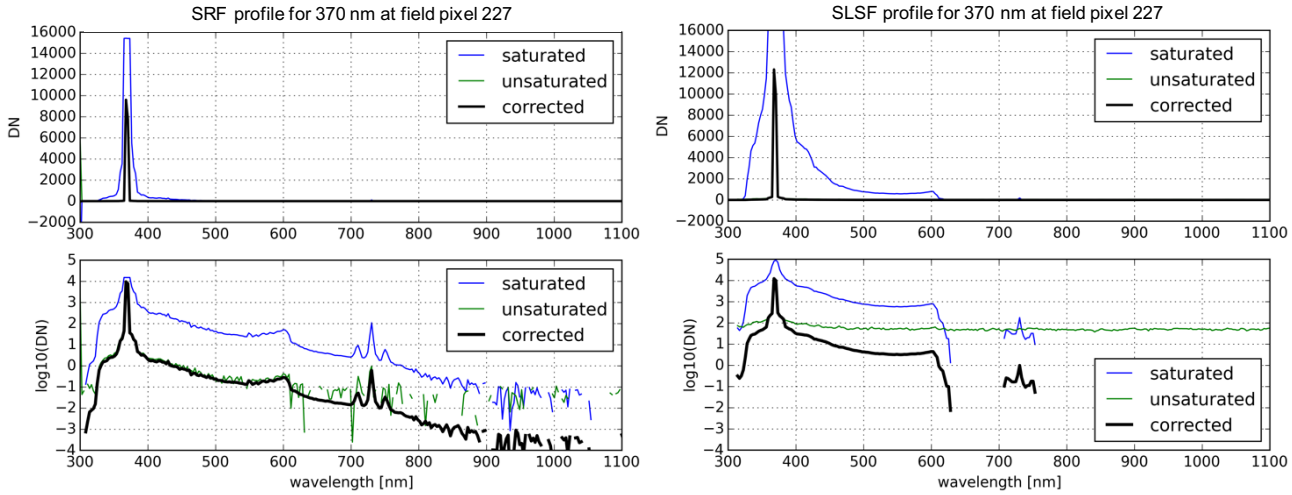

Figure 9: PRISM SRF profiles for 370 nm and field pixel 227 showing original and corrected profiles.
Top left: Saturated, unsaturated, and corrected extracted SRF profiles in DN units; *Bottom left:* Same data on $\log_{10}$ scale.
Top right: Saturated, unsaturated, and corrected summed SLSF profiles in DN units; *Bottom right:* Same data on $\log_{10}$ scale.

SRF profiles were extracted from the PSF data frames by selecting a single spatial row containing all wavelengths. This was done for each of the four measured field (spatial) pixel positions, with the results shown together in Fig. 10 (left panel). To extract the SLSF profiles, each data frame corresponding to a given field pixel was summed spatially, with the results shown together in Fig. 10 (right panel). In both cases, the profiles were normalized by their sum.

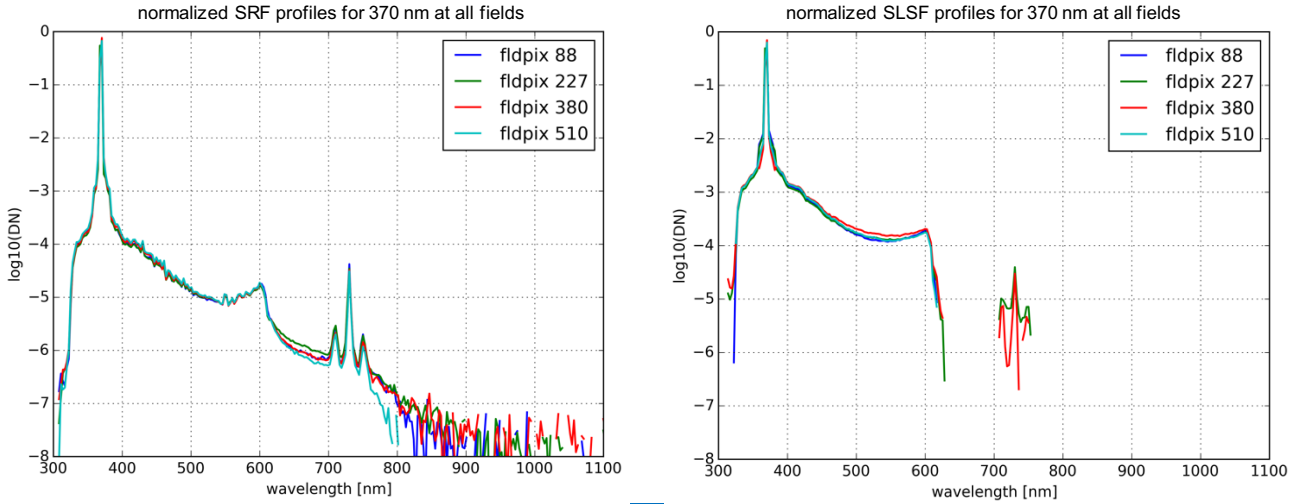

Figure 9: PRISM SRF and SLSF profiles for 370 nm and all measured field pixels.
Left: Extracted SRF profiles; *Right:* Summed (averaged) SLSF profiles.

The above procedure was performed for all eight measured wavelengths. Since the SRF and SLSF spatial variation was found to be minimal, as expected by the instrument optical design, i.e. the extracted profiles for each field position were nearly identical, these profiles were additionally averaged, with the results shown in Fig. 11.

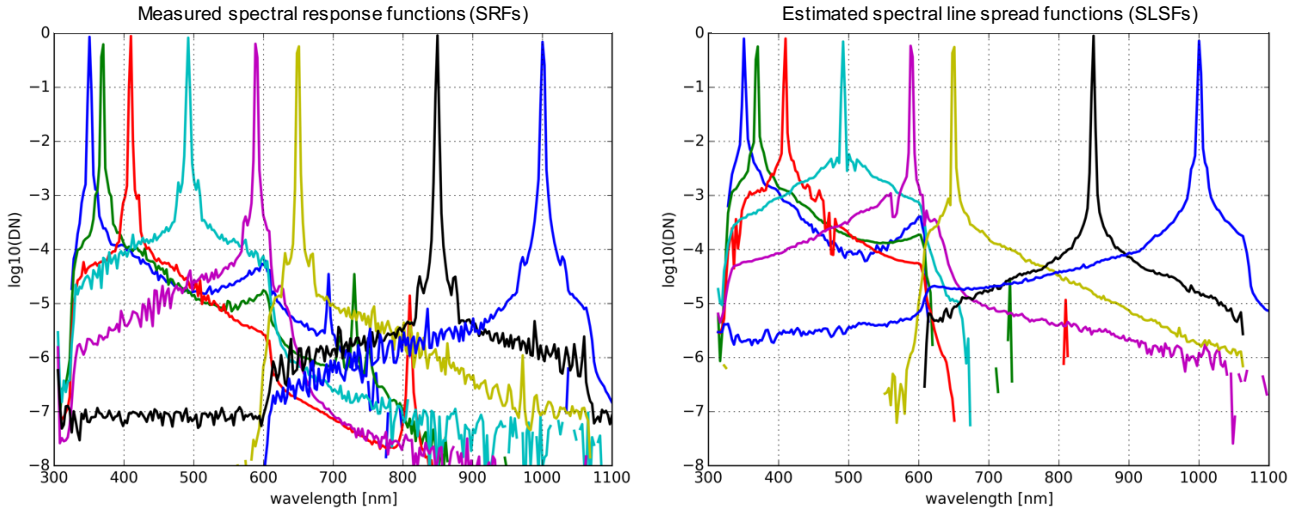

Figure 11: PRISM SRF and SLSF profiles for all measured wavelengths, averaged through field after correction procedure. *Left:* Measured SRF profiles; *Right:* Estimated SLSF profiles.

3.3 Data-derived SLSF models

To validate the spectral correction, the existing radiometric calibration method will be slightly modified. Prior to multiplication by the known panel reflectance, the measured panel DN is spatially averaged. Therefore, the SLSF, rather than SRF, will be used for the remainder of the spectral correction presented here. This allows for simple correction of existing radiometric calibration coefficients (RCCs), as well as (non-orthorectified) radiance data. Note that this does not allow for direct correction of remote sensing reflectance, since atmospheric removal is a non-linear process.

Additionally, only results using tunable laser data from the first filter segment will be presented here, since most of the retrieved reflectance error is found in the near-UV range. The second filter segment SLSF will instead use a spectral response matrix generated from previous laser line data. The eventual complete correction will repeat the described procedure using SRF and SLSF data collected for the second filter segment.

To form the spectral response matrix, knowledge of the response at all sampled wavelengths is required. Since the PSF data is spectrally sparse, i.e. only five wavelengths were collected for the first filter segment, it is not reasonable to simply interpolate through wavelength. The SRF form is nominally considered to be a sum of a narrow Gaussian response at the peak, with broader responses to account for the tails. In this case, a model for the SLSF (also applicable to the SRF) consisting of a Gaussian (peak), Lorenztian (primary stray response), two Gaussians, and an additional Lorentzian centered at the second-order dispersion position, was found to account for a significant amount of the observed spectral response (Fig. 12, left panel). This model was fit to four of the five first filter segment wavelengths (352 nm, 370 nm, 410 nm, 590 nm), with the 492 nm measurement considered an outlier and not used at this time.

Initially, each of the individual fits were compared to all other fits, with center wavelength adjusted as appropriate. Neglecting wavelength dependence of the SLSF form, the 410 nm fit was observed to be the best compromise through wavelength, and is shown in Fig. 12 (right panel). Note that second-order effects are not well accounted for by choosing a single form to represent all wavelengths.

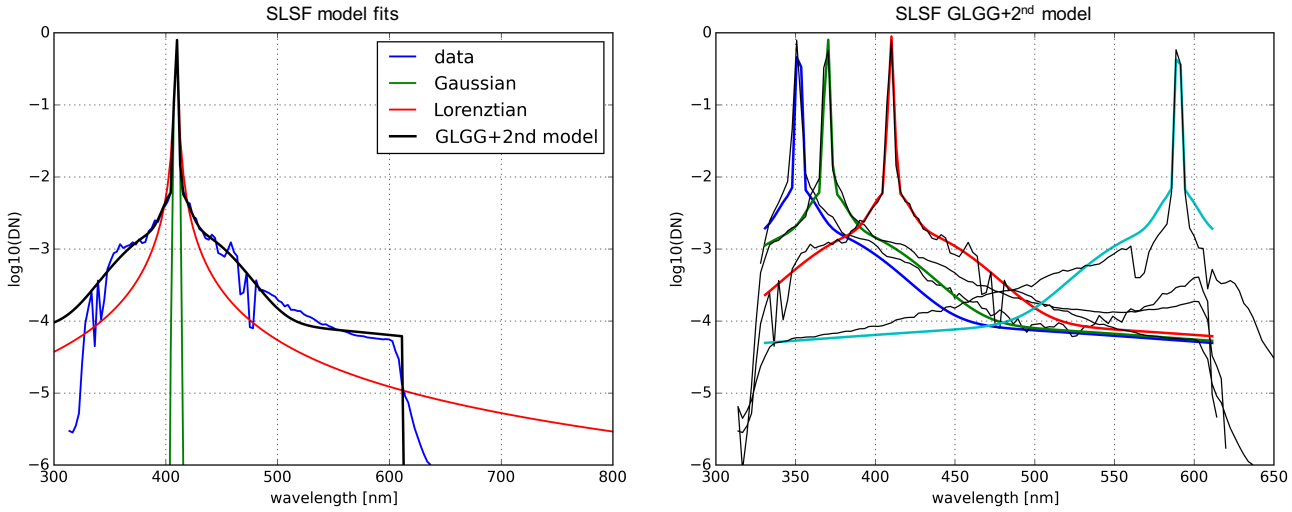

Figure 12: PRISM SLSF for the 410 nm case, where GLGG+2nd indicates the (G)aussian+(L)orenztian+G+G+2nd order L model.
Left: SLSF with single Gaussian, single Lorenztian, and GLGG+2nd model fits;
Right: SLSF 410 nm GLGG+2nd model applied to SLSF measured at three other wavelengths.

3.4 Construct SLSF matrix with wavelength dependence

The SLSF model for the 410 nm wavelength was used to construct the SLSF matrix shown in Fig. 13 (left panel). The modeled SLSF is shifted through wavelength and the new profiles are stacked such that the resultant matrix is square with dimensions corresponding to the number of sampled wavelengths in the first filter segment.

An initial simulation accounting for the wavelength dependence observed in the SRF and SLSF data (Fig. 11) used the model fit parameters for all measured wavelengths. Interpolated splines were fit to amplitude and spread parameters for the Gaussian and Lorenztian functions, with 1st order and 2nd order fits selected as appropriate. The interpolated parameters were then used to construct a SLSF matrix including wavelength dependence (Fig. 13). There are clear interpolation errors, especially in the region of highest expected SRF/SLSF variability (350 nm to 400 nm). This is partially due to insufficient PSF sampling in this range, and the interpolation underestimates the response magnitude, most notably near 370 nm. Additional tunable laser data will be collected and more sophisticated modeling approaches will be explored in the future.

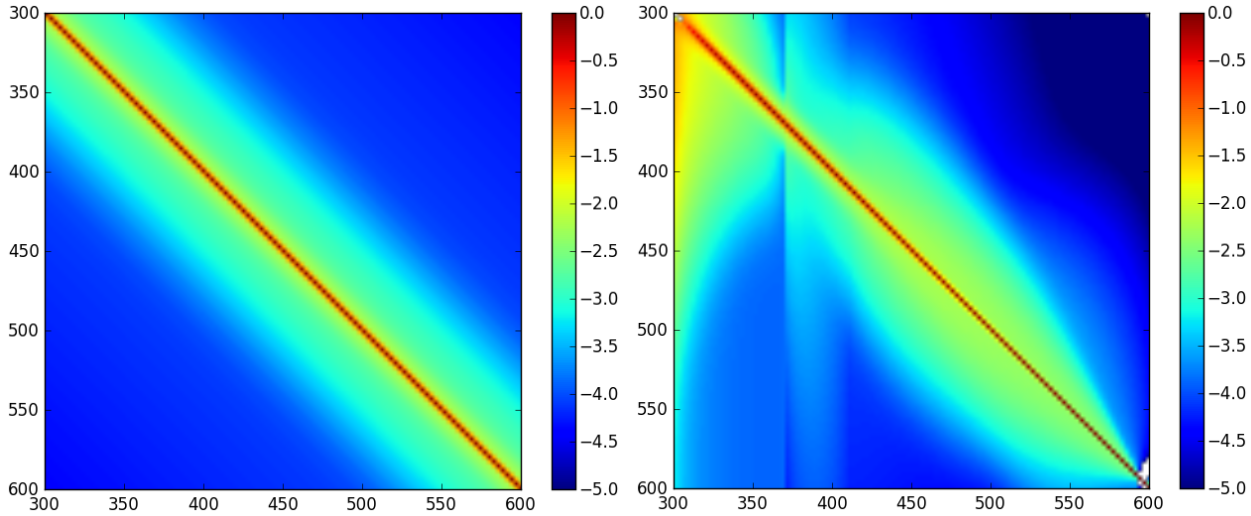

Figure 13: PRISM SLSF matrices for first filter segment
Left: SLSF matrix constructed using 410 nm model;
Right: SLSF matrix constructed using wavelength interpolated model.

4. STRAY SPECTRAL RESPONSE CORRECTION

After application of the PdS and EP corrections to raw data frames, the data are ready for radiometric calibration.

A flat field image is first generated by filling the instrument aperture with uniform illumination. In the laboratory, a standard integrating sphere and quartz tungsten halogen lamp are used [Mouroulis et al. 2014]. For instrument-in-aircraft flat field collection, a smaller integrating sphere is placed in a custom frame with a curved guide to ensure that the instrument observes identical illumination through the entire field of view (FOV).

Radiometric calibration coefficients (RCCs) are required to convert measured DNs to calibrated radiance values. A NIST-calibrated tungsten lamp of known spectral irradiance is oriented at 45 degrees from normal of a Spectralon panel of known spectral reflectance, and moved throughout the instrument FOV. For instrument-in-aircraft calibration, the lamp and panel are mounted in a box specially designed to prevent stray light from illuminating the panel. In addition, spectrally black cloth is used to cover the bottom of the aircraft, to further reduce stray light on the panel.

4.1 Radiometric calibration with spectral correction

For the standard calibration, measured panel DNs are averaged spatially and the RCC vector is calculated as:

$$RCC_{panel} = \frac{L_{panel}}{DN_{panel}} \tag{4.1}$$

For the stray spectral response corrected calibration, the correction in Eq. (3.2) is applied directly to DN_{panel} (in place of L_{meas}) where $C = I$ and S is the stray SLSF (SSLSF) matrix in this case. That is, the nominal Gaussian response from the SLSF (NSLSF) is neglected, so that only the SSLSF remains. This maintains the ability to use existing downstream processing algorithms, including those for atmospheric removal.

For comparison between original and uncorrected RCCs (Fig. 14), it is instructive to calculate the ratio of coefficients as:

$$RCC_{ratio} = \frac{RCC_{panel}}{RCC_{corr}} \tag{4.2}$$

where the subscript *corr* indicates the post-spectral response corrected RCCs.

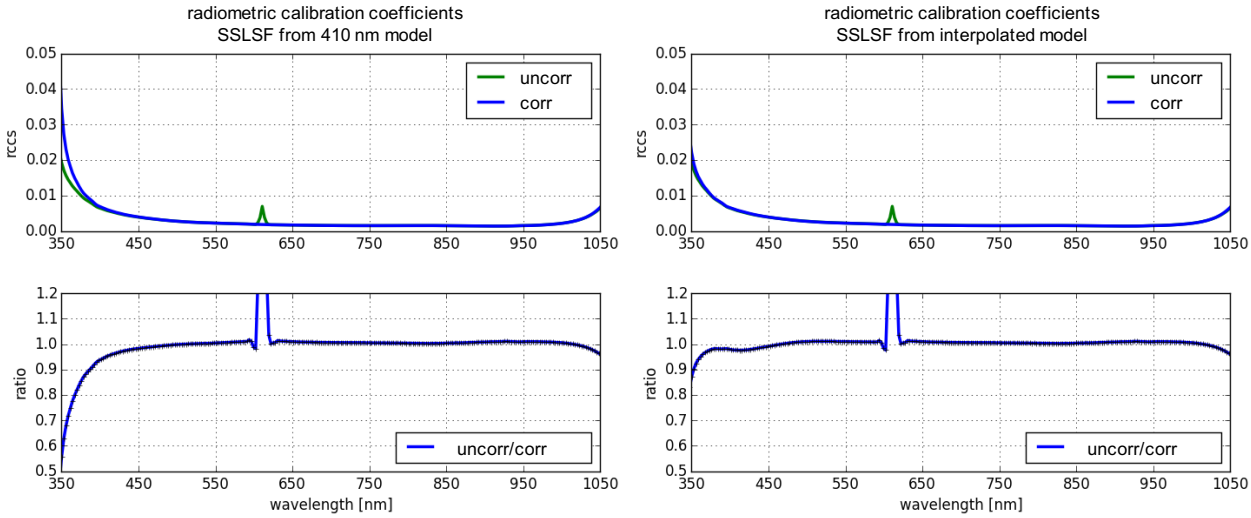

Figure 14: PRISM radiometric calibration coefficients and uncorrected/corrected ratios
Left: Corrected with SSLSF matrix constructed using 410 nm model;
Right: Corrected with SSLSF matrix constructed using wavelength interpolated model.

4.2 Field data calibration

A PRISM spectral profile was extracted from a Kaneohe Bay Marine Corps Air Station tarmac scene (Fig. 15). Multiple ground truth data sets were collected, with colored text indicating measurement regions.

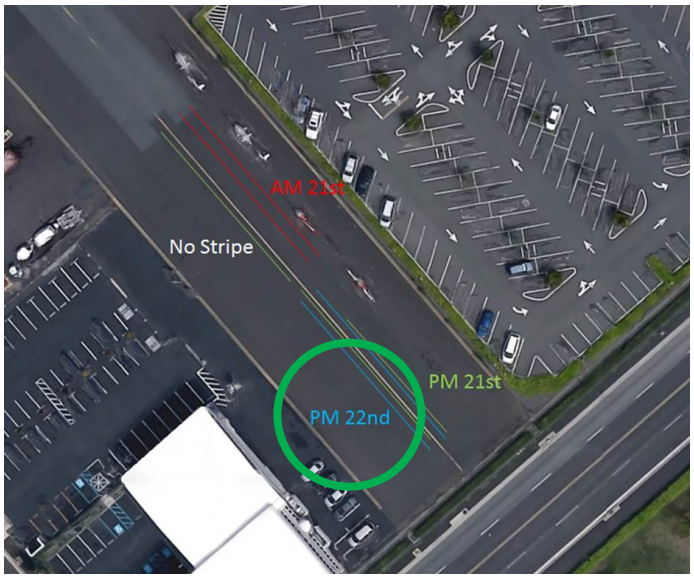

Figure 15: PRISM spectral radiance profiles selected from airport tarmac scene.
Green circle represents region of interest for the present study.

To complete the calibration, the RCCs are combined with the flat field image and multiplied by subsequently measured DNs in a single step, yielding calibrated, spectral response corrected radiance values:

$$L_{meas} = RCC_{panel} DN_{meas} \tag{4.3}$$

Fig. 16 compares the calibrated radiance result with and without spectral correction of the RCCs.

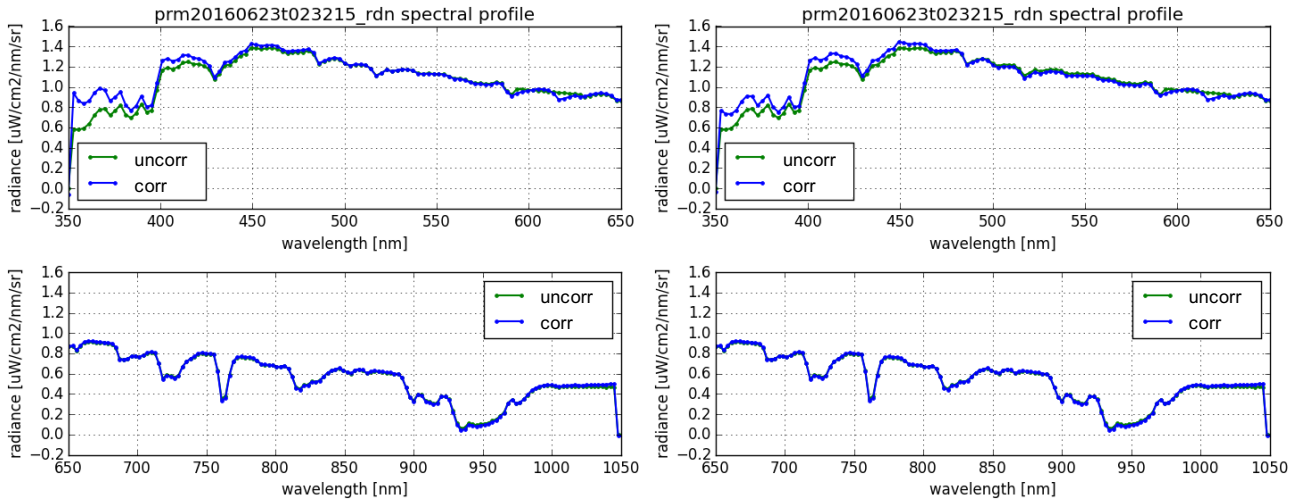

Figure 16: PRISM spectral radiance profiles selected from airport tarmac scene
Left: Corrected with SSLSF matrix constructed using 410 nm model;
Right: Corrected with SSLSF matrix constructed using wavelength interpolated model.

Note that for a full spectral correction, DN_{meas} must also be corrected using the procedure described by Eq. (3.2). However, field data is not typically spatially averaged, so the SSRF must be used directly, i.e. the SLSF no longer applies. Correcting DN_{meas} will reduce the estimated spectral radiance, since stray spectral light at each pixel is minimized. In many cases, including the present example, this has a much smaller effect than that of using uncorrected RCCs. However, in regions of high spectral variability, e.g. coral reefs, the full correction should be performed.

4.3 Convert radiance L to remote sensing reflectance R_{RS}

After calculation of calibrated radiance, science data processing typically proceeds to orthorectification and atmospheric estimation and removal [Gao et al. 2000], including division by solar irradiance, which also requires special consideration due to sharp variation in the near-UV region.

The selected validation site is a region of low reflectance, spectrally flat airport tarmac indicated by the green circle in Fig. 15. This region was selected due to relative ease of frequent overflights and accessibility for the ground measurement team. Fig. 17 indicates that the ground truth reflectance (green lines), collected using an ASD FieldSpec Pro spectrometer, was approximately 4% and highly uniform over the measured spectral range.

The PRISM retrieved reflectance profiles (blue lines) are a reasonable match to the ground truth measurement, with an overall error offset of ~10%. Without performing the stray spectral correction, error in the near-UV region rapidly increases to greater than 60% at 350 nm. Using the SSLSF 410 nm model correction, error in the same region drops to nearly 0%. Using the SSLSF wavelength interpolated model correction, the error is not as well-corrected. In principle, this model should be more accurate, but there exist significant interpolation errors as shown in Fig. 13. (right panel).

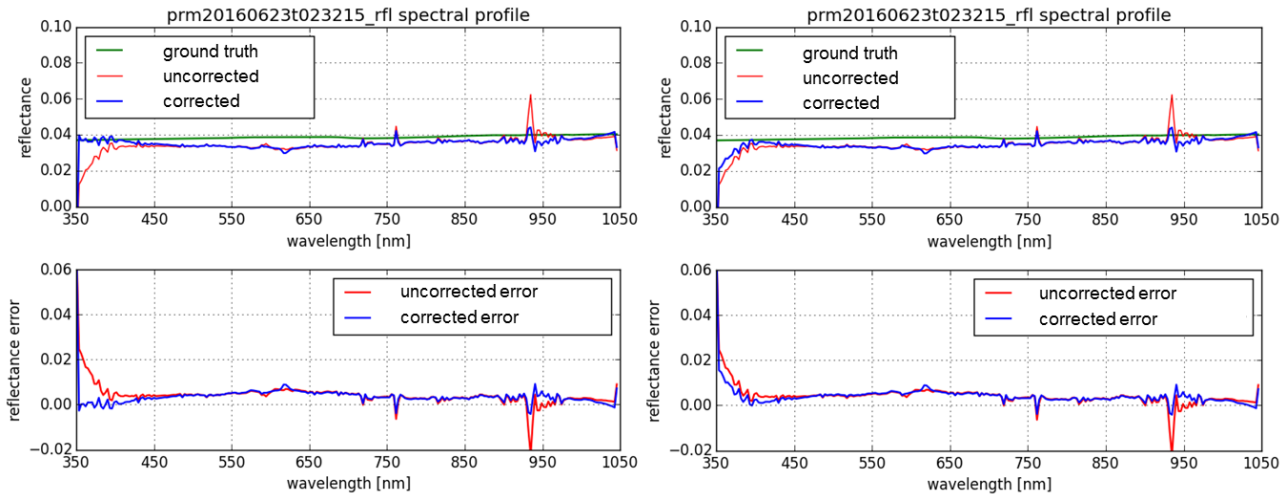

Figure 17: PRISM spectral reflectance profiles selected from airport tarmac scene (Fig. 15)
Left: Corrected with SSLSF matrix constructed using 410 nm model;
Right: Corrected with SSLSF matrix constructed using wavelength interpolated model.

5. CONCLUSIONS

The procedure for PRISM science data processing, from raw to reflectance, has been described in detail. Starting with raw data, the pedestal shift (PdS) and electronic panel (EP) artifact corrections are applied. The instrument spectral response characteristics are estimated and used to correct stray spectral response. Completion of the flat field and radiometric calibration steps yield corrected, calibrated radiance L_{corr} values. Following orthorectification and atmospheric removal, remote sensing reflectance R_{RS} is retrieved. R_{RS} can be validated against ground truth measurements and used in subsequent processing algorithms, such as benthic reflectance retrieval.

For the SSLSF correction using the 410 nm model, there appears to be a slight overcorrection in the near-UV and near-IR regions, given the overall level of reflectance observed at the other, mostly unchanged, wavelengths. This may be a result of not accounting for the stray spectral response in DN_{meas}. For the SSLSF correction using the wavelength interpolated model, the near-UV and near-IR regions appear to be under-corrected. However, since the SSLSF interpolated matrix exhibits significant artifacts due to under-sampling of the input SLSF data, a strong conclusion cannot yet be made. Future efforts will involve collecting PSF data at more center wavelengths throughout the 350 to 400 nm range, in order to better inform the interpolation of model parameters. An alternate approach is to develop a physically-based model that takes into account knowledge of grating scatter, order-sorting filter dropoff, and second order effects.

Note that the ASD spectrometer has been observed to have significant stray spectral response (unpublished data), but this has not been fully investigated. If this is indeed the case and the ASD data is also spectrally corrected, the overall level of measured ground truth reflectance would be expected to decrease, with any spectral differences in ASD PSF/SRF form contributing to wavelength dependent variation. In any case, extreme care should be taken when comparing measurements from different spectroscopic instruments.

There are also strategies for connecting simple sets of measurements to the initially characterized SRF, in order to track changes in the field over time. A long-pass filter transmission method [Kohler et al. 2004] has been explored that could use the SLSF described in the present study. Laser line measurements offer another option and are easily collected using an integrating sphere. Tunable laser measurements are time consuming and may only be reasonable to collect infrequently, and only in the laboratory.

The present study only described the correction of the stray spectral response. From Eq. (3.2), it is clear that a complete correction also requires removal of stray cross-track response. Efforts to characterize the cross-track response function (CRF) are in progress, but preliminary results indicate both spatial and spectral dependence. This violates the assumption of PSF separability that yielded Eq. (3.1) and, in turn, Eq. (3.2). Therefore, a full PSF correction may be required, which would require novel processing methods to avoid a pixel-by-pixel correction of each data frame.

When introducing the stray response correction (SRF, CRF, and/or PSF) into the general science data processing stream, the best approach is likely to do so as a parallel set of data products. This would allow end users to easily choose whether or not to utilize the corrected data. In many cases, researchers develop their own set of algorithms and processes for post-radiance processing that may expect certain characteristics to be present in the data, e.g. nominal Gaussian response. The current method of preserving the NSRF attempts to avoid this issue, but some downstream effects may be unpredictable.

Finally, to have high confidence in any stray response correction, the as must be validated on real-world data sets. The low reflectance, spectrally uniform tarmac data offered a promising initial result. However, similar tests must be performed on diverse scenes, especially those with high spectral and spatial variability, e.g. coral reef and sea ice regions.

ACKNOWLEDGMENTS

The research in this paper was performed at the Jet Propulsion Laboratory, California Institute of Technology under contract with the National Aeronautics and Space Administration. Reference herein to any specific commercial product, process, or service by trade name, trademark, manufacturer, or otherwise, does not constitute or imply its endorsement by the United States Government or the Jet Propulsion Laboratory, California Institute of Technology. We thank Michael Eastwood and Dan Ryan for assistance operating the tunable laser system, and Robert Green and Scott Nolte for collection of ground truth measurements.

REFERENCES

[1] Mouroulis, P., Van Gorp, B., Green, R.O., Dierssen, H., Wilson, D.W., Eastwood, M., Boardman, J., Gao, B.C., Cohen, D., Franklin, B. and Loya, F., 2014. Portable Remote Imaging Spectrometer coastal ocean sensor: design, characteristics, and first flight results. *Applied Optics*, 53(7), pp.1363-1380.

[2] Thompson, D.R., Hochberg, E.J., Asner, G.P., Green, R.O., Knapp, D., Gao, B.-C., Garcia, R., Gierach, M., Lee, Z., Maritorena, S., and Fick, R., 2017. Airborne mapping of benthic reflectance spectra with Bayesian linear mixtures. *Remote Sensing of Environment* (in press).
[3] E. E. Heupel, K. Bostrom, Z. Mouroulis, R. Green, B. Gao, and H. M. Dierssen: Hyperspectral Remote Sensing in Coastal Regions: PRISM Field Validation in Elkhorn Slough. *Ocean Optics XXI.* (TOS). Glasgow Scotland. (October 2012).
[4] Stephens, B., Long, M., Keeling, R., Kort, E., Sweeney, C. et al., 2017. The O2/N2 ratio and CO2 airborne Southern Ocean (ORCAS) study. *Bulletin of the American Meteorological Society.* (in press).
[5] Green, R.O., 1998. Spectral calibration requirement for Earth-looking imaging spectrometers in the solar-reflected spectrum. *Applied Optics*, 37(4), pp.683-690.
[6] NASA CORAL mission, http://coral.jpl.nasa.gov/.
[7] Thompson, D.R., Boardman, J.W., Eastwood, M., Green, R.O., Haag, J.M., Mouroulis P., and Van Gorp, B.E., 2017. Imaging spectrometer stray spectral response: In-flight characterization, correction, and validation. *Submitted*.
[8] Zong, Y., Brown, S.W., Johnson, B.C., Lykke, K.R. and Ohno, Y., 2006. Simple spectral stray light correction method for array spectroradiometers. *Applied Optics*, *45*(6), pp.1111-1119.
[9] Gao, B.-C., Montes, M.J., Ahmad, Z. and Davis, C.O., 2000. Atmospheric correction algorithm for hyperspectral remote sensing of ocean color from space. *Applied Optics*, *39*(6), pp.887-896.
[10] Kohler, D.D., Bissett, W.P., Steward, R.G. and Davis, C.O., 2004. New approach for the radiometric calibration of spectral imaging systems. *Optics Express*, *12*(11), pp.2463-2477.